A Framework to Evaluate Convective Aggregation: Examples with Different Microphysics Schemes

Jin-De Huang[1] and Chien-Ming Wu[1]

[1]National Taiwan University

November 22, 2022

Abstract

This study introduces a framework to evaluate convective aggregation (CA) under radiative-convective equilibrium simulations using the vector vorticity equation cloud-resolving model (VVM) coupled to a mixed-layer slab ocean. The framework introduces the competing effects between the convection-SST feedback (CSF) and the moisture-convection feedback (MCF) by modifying the initial SST gradient and the mixed layer depth. Examples of applying this framework are demonstrated by comparing simulations with different microphysics schemes. The convectional five-category scheme (VVM-Lin) and the predicted particle properties scheme (P3) are examined by the matrix formed by these two factors. A clear bifurcation of the aggregated/non-aggregated states can be identified in both sets of experiments. The change of the bifurcation between two sets of experiments suggests that the P3 experiments tend to develop CA due to the stronger MCF. The budget analysis of spatial frozen moist static energy variance is applied to quantify the stronger MCF in the P3 simulations. Convective systems in P3 simulations develop more organized structures, which enhances MCF and leads to CA. The proposed framework provides a reconciled view of the process-based evaluation of CA among cloud-resolving models that use different dynamics and physical parameterizations.

A Framework to Evaluate Convective Aggregation: Examples with Different Microphysics Schemes

Jin-De Huang and Chien-Ming Wu

Department of Atmospheric Sciences, National Taiwan University, Taipei, Taiwan

Corresponding authors: Chien-Ming Wu (mog@as.ntu.edu.tw)

Key points

- A framework is designed for evaluating convective aggregation (CA), focusing on two competing feedbacks in cloud-resolving models.
- A clear bifurcation of the aggregated/non-aggregated states can be identified in experiments with different microphysics.
- P3 experiments tend to develop CA due to the stronger MCF owing to more organized convective systems.

Abstract

This study introduces a framework to evaluate convective aggregation (CA) under radiative-convective equilibrium simulations using the vector vorticity equation cloud-resolving model (VVM) coupled to a mixed-layer slab ocean. The framework introduces the competing effects between the convection-SST feedback (CSF) and the moisture-convection feedback (MCF) by modifying the initial SST gradient and the mixed layer depth. Examples of applying this framework are demonstrated by comparing simulations with different microphysics schemes. The convectional five-category scheme (VVM-Lin) and the predicted particle properties scheme (P3) are examined by the matrix formed by these two factors. A clear bifurcation of the aggregated/non-aggregated states can be identified in both sets of experiments. The change of the bifurcation between two sets of experiments suggests that the P3 experiments tend to develop CA due to the stronger MCF. The budget analysis of spatial frozen moist static energy variance is applied to quantify the stronger MCF in the P3 simulations. Convective systems in P3 simulations develop more organized structures, which enhances MCF and leads to CA. The proposed framework provides a reconciled view of the process-based evaluation of CA among cloud-resolving models that use different dynamics and physical parameterizations.

1 Introduction

Radiative convective equilibrium (RCE) is a conceptual model that describes a statistical balance between radiative cooling and convective heating in the atmosphere column without lateral energy transports. The concept has been applied in numerical simulations with cloud-resolving resolutions when computational resources were affordable (Held et al., 1993; Tompkins and Craig, 1998). In these studies, sometimes convection spontaneously aggregates from a random spatial distribution to clustered systems surrounded by dry convection-free areas despite spatially homogeneous and temporally constant sea surface temperature (SST). This process, called convective self-aggregation (CSA), largely changes environment moisture distribution and radiative energy due to the expansion of dry areas (Holloway and Woolnough, 2016; Wing et al., 2017). The enhanced cooling effect of outgoing longwave radiation due to CSA is regarded as a process that could reduce climate sensitivity (Khairoutdinov and Emanuel, 2010; Mauritsen and Stevens, 2015), and its impacts on the tropical climate have been examined and discussed (Cronin and Wing, 2017; Holloway et al., 2017; Wing, 2019).

Wing et al. (2018) organized the Radiative-Convective Equilibrium Model Intercomparison Project (RCEMIP) to investigate the roles of clouds and CSA in climate sensitivity. The RCEMIP ensemble results show that responses of the raised cloud top height and reduced high cloud coverage to the warming robustly across several types of models (Wing et al., 2020). Despite many similar behaviors to the warming found in models, there are large differences in thermodynamic structures, the degree of CSA, and the sensitivity of CSA to SST between models. The diverse outcomes in RCEMIP among models could be expected because of sophisticated interactions between physical and dynamical processes, especially in the cloud-resolving models. The numerical setups in previous studies have an impact on the occurrence of CSA due to the sensitivity of convection to the physical treatments, boundary conditions, or model configurations. Using a general circulation model, Coppin and Bony (2015) revealed that the leading process driving the development of CSA is sensitive to SST, and the longwave radiation and the wind-induced surface heat exchange mechanism are critical in high and low SST conditions, respectively. Holloway and Woolnough (2016) showed that CSA develops faster when the rain evaporation is off, and fixed surface enthalpy fluxes and radiative cooling lead to the non-aggregated equilibrium states. Tompkins and Semie (2016) found that the treatment of the sub-grid turbulence mixing can change the behavior of CSA, and high entrainment rates in the dry regions prohibit the development of convection, which leads to the occurrence of CSA. Muller and Held (2012) found that the occurrence of self-aggregation is related to the horizontal scale of the simulated domain, and Yanase et al. (2020) identified the critical length scale for CSA, which is controlled by the competition between large-scale subsidence and cold pool propagation. The above studies suggest that CSA is sensitive to various factors, some of which depend on the models themselves. It is not surprising that there are miscellaneous responses to the warming in the RCEMIP, and understanding the cause of the spread in RCEMIP is essential for evaluating the impacts of CSA on the tropical climate.

Numerous physical processes have been identified as potentially important to the initiation and maintenance of CSA in cloud-resolving simulations (detail reviews in Wing et al., 2017 and Holloway et al., 2017). The interactions between longwave radiation, water vapor, and clouds were found to be critical for CSA (Muller and Held, 2012; Holloway and Woolnough, 2016), while the wind-induced surface fluxes exchange mechanism plays an important role in the warm SST conditions (Coppin and Bony, 2015). However, these diabatic processes are not always essential for CSA (Tompkins, 2001). The interaction between convection and moisture can also trigger and maintain the CSA in the simulations with prescribed radiative or surface fluxes (Grabowski and Moncieff, 2004; Muller and Bony, 2015). This is because the convection-induced subsidence dries the nearby atmosphere and suppresses the convection development there, while convection moistens its own environment and favors convection due to the reduction of entrainment (Tompkins, 2001; Grabowski and Moncieff, 2004; Holloway and Neelin, 2009; Tompkins and Semie, 2016). This interaction is known as moisture-convection feedback (MCF, Grabowski and Moncieff, 2004) that enhances the spatial differences in moisture through the circulation generated by convection. On the other hand, MCF can also be described by idealized models with simplified physical processes. Craig and Mack (2013) demonstrated that the theoretical model of the coarsening process captures a similar behavior of the development of CSA with MCF. Emanuel et al. (2014) have shown that RCE instability occurs when subsidence and convection can effectively, respectively, dry and moisten atmospheric columns. Both cloud-resolving simulations and idealized models suggest that MCF seems to be a fundamental mechanism for CSA.

In cloud-resolving simulations with spatially uniform SST, MCF could be randomly triggered by many factors, such as the spatial variability of convection and inhomogeneities of surface fluxes. To assess the role of MCF, we adopt a spatial SST gradient distribution in the experimental design. The approach has been applied to mimic Walker or Hadley circulation in both cloud-resolving simulations and simplified models for understanding the behaviors of the large-scale flow (Grabowski et al., 2000; Bretherton and Sobel, 2002; Liu and Moncrieff, 2008; Wosfy and Kuang, 2012; Byrne and Schneider, 2016; Chen and Wu, 2019). When the SST gradient is prescribed (Fig. 1a), the convection will be induced in the warmer region and then drive a mock-Walker circulation (blue arrow in Fig. 1a), and the subsidence of the mock-Walker circulation dries the column over the colder SST region (Grabowski and Moncrieff, 2001; Bretherton et al., 2006). MCF induced by the mock-Walker circulation brings the evolution towards the aggregated state, and the convection no longer aggregates spontaneously. The design prevents uncertain triggering mechanisms of convective aggregation (CA) among cloud-resolving models. Another advantage is that the treatment of physics and dynamics can be regarded as the impacts on the mock-Walker circulation because MCF is the leading mechanism for CA.

The prescribed SST gradient forces the equilibrium towards the aggregated state across the simulation. This constant-in-time forcing would diminish the effects of other processes during the development of CA. Besides, convection in the simulations with the prescribed SST gradient rapidly develops to the equilibrium with CA within few days, which leads to difficulties in analyzing and discussing the impacts of slow physical processes such as radiation. To eliminate the flaws of the prescribed SST gradient, we introduce a mixed-layer slab ocean in our framework. With the interactive SST, CA is delayed or broken down because of air-sea coupling (Bretherton et al., 2005; Reed et al., 2015; Hohenegger and Stevens, 2016; Chen and Wu, 2019; Tompkins and Semie, 2021), also known as convection-SST feedback (CSF, Grabowski, 2006). As the time proceeds following the scenario in Fig. 1a with the interactive SST, convection will reduce the shortwave radiative heating of the ocean and enhance wind-induced surface fluxes, and both processes cool SST in the convective region. On the other hand, SST in the clear region is heated due to shortwave radiative heating. Then, the SST gradient is reversed as shown in Fig. 1b and induced a low-level circulation (red arrow in Fig. 1b) that counteracts the mock-Walker circulation. The opposed low-level circulation flattens the spatial enthalpy differences in the low levels through the advection and leads to the non-aggregated equilibrium state.

In the experimental design, whether CA develops or not depends on the competition between MCF and CSF. Following Chen and Wu (2019), MCF is represented by a zonally bell-shaped SST distribution initially prescribed in the slab ocean, and a larger SST gradient favors stronger MCF. CSF is controlled by the depth of the mixed-layer slab ocean model. With a shallow ocean mixed-layer depth, SST can respond faster to radiative heating compared to a deep one. The boundary layer circulation builds up faster to counteract the development of CA. By modifying the strength of MCF and CSF, we can construct a phase diagram with MCF and CSF to evaluate CA. In this study, we provide examples of two different microphysics schemes using this framework. The rest of this paper is organized as follows. Section 2 provides the details of the experimental settings. The results of applying the framework are presented in section 3. We discuss the possible mechanism associated with different microphysics in section 4. A summary section is presented in section 5.

2 Model description, experimental settings, and analyses methods

2.1 The model and experiment setup

The model used in this study is the vector vorticity equation cloud-resolving model (VVM, Jung and Arakawa, 2008). Horizontal components of anelastic vorticity equations are predicted in the VVM, and velocities are diagnosed through solving a three-dimensional elliptic equation. The use of the vorticity equations eliminates pressure gradient force and inherently couples the dynamics to the thermodynamics in the governing equation. The unique dynamical core of VVM can better capture the circulation associated with the thermal gradient. The radiation model (RRTMG, Iacono et al., 2008), the land surface model (Noah LSM, Chen and Dudhia, 2001), the predicted particle properties microphysical scheme (Morrison and Milbrandt, 2015; Huang and Wu, 2020), and the block topography (Wu and Arakawa, 2011; Chien and Wu, 2016) has been implemented in the VVM for studying complicated interactions associated with convection, such as the unified parameterization of deep convection (Arakawa and Wu, 2013; Wu and Arakawa, 2014), stratocumulus transition (Tsai and Wu, 2016), the aggregated deep convection (Tsai and Wu, 2017), afternoon thunderstorms (Kuo and Wu, 2019), land-atmosphere interactions (Wu et al., 2015; Wu et al., 2019; Wu and Chen, 2021), cloud-aerosol interactions (Chang et al., 2021), and the coastal convection during summer monsoon onset (Chen et al., 2019).

Two sets of experiments are performed using VVM with a conventional predefined-ice-category microphysical parameterization (VVM-Lin, Krueger et al., 1995) and the predicted particle properties microphysics schemes (P3, Morrison and Milbrandt, 2015; Huang and Wu, 2020). The horizontal domain is 1024×256 km^2 with the 2 km resolution, and the vertical resolution stretches from 100 m at the bottom and to around 1 km at the model top at 30 km. The slab mixed-layer ocean model coupled to VVM predicts SST using an energy budget equation following Chen and Wu (2019), and the initial SST gradient is given as a perturbation of a cosine function on the mean SST of 300 K. The dynamical fields are nudged to the calm state with the timescale of 1 day to prevent the shifting of the moist region that reported in previous channel RCE studies (Wing and Cronin, 2016; Wing et al., 2020). The experiment names are abbreviated with their microphysics, initial SST gradient, and mixed layer depth, as listed in Table 1. Most of the simulations are integrated for 25 days because reaching equilibrium quickly, and some simulations with the slow development of CA is integrated until 50 days to ensure consistent result after the onset of CA, which will be defined later. Besides, the suffix of -all represent the entire set with the same microphysics, and the suffixes of -agg and -no-agg indicate the simulations with and without CA, respectively.

2.2 Moist static energy variance budget

To evaluate the impacts of physical processes on CA, we apply the budget of the spatial variance of column-integrated frozen moist static energy introduced by Wing and Emanuel (2014). The frozen moist static energy (FMSE) is conserved by considering ice microphysical processes during moist adiabatic processes, and it is defined as

$$h_f \equiv c_p T + gz + L_v q_v - L_f q_i. \quad (1)$$

In eq. (1), L_v and L_f are the latent heat of vaporization and freezing, respectively; q_v and q_i are the mixing ratio of water vapor and ice-phase condensates, respectively; T and z are the temperature and height of the air; c_p is the specific heat capacity of dry air at constant pressure, and g is the gravitational acceleration constant. Through vertical integration weighted with density, the vertical redistribution term within the atmosphere column is eliminated, and the sources and sinks occur at the top and bottom boundaries and lateral transport. The budget for column FMSE is written as

$$\frac{\partial \widehat{h_f}}{\partial t} = \mathrm{SW} + \mathrm{LW} + \mathrm{SEF} - \nabla_h \cdot \widehat{\vec{u}h_f}. \quad (2)$$

In eq. (2), $\widehat{h_f}$ is column-integrated FMSE; SW and LW refer to the convergence of shortwave and longwave radiative fluxes between surface and top of the atmosphere, respectively; SEF is surface enthalpy flux; and $\nabla_h \cdot \widehat{\vec{u}h_f}$ represents the horizontal divergence of column FMSE flux. Through linearizing eq. (2) and multiplying with $\widehat{h_f}'$, we can yield the budget equation of spatial FMSE variance

$$\frac{1}{2}\frac{\partial \widehat{h_f}'^2}{\partial t} = \widehat{h_f}' \left[SW' + LW' + SEF' - \nabla_h \cdot \widehat{\vec{u}h_f}' \right]. \quad (3)$$

In eq. (3), positive covariance terms imply that the certain process contributes to the increase of spatial FMSE variance and enhances the development of CA. The budget analysis is calculated based on daily-averaged model output, and the residual from the budget equation is taken into the FMSE divergence term.

3 Results

3.1 Bifurcation of convective aggregation

The evolutions of the competition between MCF and CSF are qualitatively demonstrated by the time evolution of the horizontal distribution of daily-averaged mass streamfunction, frozen moist static energy (FMSE), and SST in the simulations with and without the development of CA as shown in Fig. 2. We present experiments P3-1.5K-0.5m and P3-1.5K-2.0m that have drastic differences in the evolution of CA as the mixed-layer depth is changed. On day 1, the mock-Walker circulation is induced in both simulations, and the subsidence dries mid-troposphere (600 hPa) as seen in the FMSE. Both simulations have similar responses to the initial SST gradient, but the mock Walker circulation is weaker in P3-1.5K-0.5m due to stronger CSF in which the shallower mixed-layer depth results in the faster flattening of the initial zonal SST gradient. The stronger CSF in P3-1.5K-0.5m outweighs MCF, and the mock-Walker circulation cannot be maintained on day 5. P3-1.5K-0.5m has zonally similar values of daily-averaged OLR and homogeneous FMSE distribution in the domain, which indicates convection develops sporadically instead of being confined around the domain center. On day 9, the situation is consistent with the result on day 5 in P3-1.5K-0.5m. In P3-1.5K-2.0m, the convection continues to develop in the center of the domain producing strong circulation, which leads to low values of daily-averaged OLR and a large horizontal gradient in FMSE. Notably, the equilibrium states of the two experiments are similar to their states on day 9. This suggests that the competition between MCF and CSF occurs in the first several days and determines whether or not CA develops.

We use the variance of column-integrated FMSE deviated from the spatial mean to quantify CA (Wing and Emanuel, 2014; Holloway and Woolnough, 2016; Wing et al., 2017;

Wing et al., 2020). The time evolutions of the domain-averaged FMSE variance for all simulations are presented in Fig. 3a. The experiments bifurcate into two groups after day 10, in which one group reaches an equilibrium state with the large FMSE variance, while the other one undergoes the decrease of the FMSE variance and then remains lower FMSE variance. MCF dominates in the former group of the simulations and leads to CA similar to P3-1.5K-2.0m, while CSF dictates and results in the non-aggregated equilibrium in the other group like P3-1.5K-0.5m. The occurrences of CA are defined as the domain-averaged FMSE variance greater than 10^{15} J^2 m^{-4} (Table 1), and they are summarized in the phase diagram composed of the initial SST gradient and the mixed-layer depth (Fig. 3b). The dashed lines of VVM-Lin-all and P3-all indicate the bifurcation of aggregated/non-aggregated states. The fact that these two sets of simulations exhibiting different bifurcation lines is a clear demonstration that our framework can effectively identify how the two feedbacks compete with each other during the development of CA among different models. The bifurcation line of P3-all is located at the lower-left part of the phase diagram, which indicates stronger MCF in P3-all compared to that in VVM-Lin-all. The results show that the framework provides a process-based evaluation of CA with different model physics, and the sophisticated interactions between physical processes can then be simplified to the impacts on the mock-Walker circulation.

3.2 Evaluations with FMSE variance budget

The budget analysis of the FMSE variance is applied to investigate the physical processes that lead to enhanced MCF in P3-all. The day that the domain-averaged FMSE reaches 10^{15} J^2 m^{-4} is defined as the onset of CA, and it ranges from 5 to 25 days in all the aggregated simulations (Table 1). Small variations of the onset definition do not affect the interpretations of the results. The budget terms are the summations before the onset day, as shown in Fig. 4. In this way, we can evaluate the contributions from various processes while the total tendency terms of the FMSE variance budget are similar in these simulations. The contributions of shortwave (0.05×10^{15} J^2 m^{-4}) and longwave radiation (0.1×10^{15} J^2 m^{-4}) to FMSE variance are similar in both sets of experiments. The magnitude is relatively minor compared to the convergence terms of 0.2×10^{15} J^2 m^{-4} in VVM-Lin-agg and 0.45×10^{15} J^2 m^{-4} in P3-agg. The convergence term is dominant in the total tendency of the spatial FMSE variance. We interpret the positive convergence term as the effects of MCF. The results indicate that enhanced MCF induced by the mock-Walker circulation leads to CA developing easier in P3-all compared to VVM-Lin-all.

An interesting feature in the FMSE variance budget is found in the surface enthalpy flux term. In VVM-Lin-agg, the surface enthalpy flux term mostly enhances the increase of the horizontal FMSE variance, while it plays a negative role in the development of CA in P3-agg. The conflicting effects of the surface enthalpy flux term have been discussed in Wing and Emanuel (2014) by decomposing this term into wind anomalies, air-sea imbalance, and non-linear terms. The wind speed in the moist region (positive h') is greater than that in the dry region, and the products of the two in both moist and dry regions produce positive contributions to the spatial FMSE variance. On the other hand, the air-sea disequilibrium in the dry region is larger than that in the moist region, which leads to the larger (smaller) surface enthalpy flux in the dry (moist) region. This process is similar to the low-level circulation triggered by the reverse SST gradient (Fig. 1b), and the air-sea imbalance term could represent the effects of CSF, which counteracts to CA. Fig. 4 shows that the wind speed anomaly terms are positive in both VVM-Lin-agg and P3-agg, and the wind speed anomaly term in VVM-Lin-agg (0.17×10^{15} J^2 m^{-4}) is slightly higher than that in P3-agg (0.12×10^{15} J^2 m^{-4}). The difference in the air-sea imbalance term is significant between VVM-Lin-agg (-0.13×10^{15} J^2 m^{-4}) and P3-agg (-0.23×10^{15} J^2 m^{-4}). The reason is that the stronger circulation in P3-agg enhances the surface enthalpy fluxes in the dry region, which leads to stronger CSF. However, the effects of CSF are not enough to defeat the stronger MCF generated by the mock-Walker circulation, and the negative air-sea disequilibrium would be the result of the stronger circulation.

4 Discussion

In this framework, different treatments of microphysics might lead to changes in the convection structure that leads to changes in the bifurcation diagram. From observation, Chen et al. (2021) showed that the large-size convective systems are highly coupled with the seasonal cycle of the Asian-Australian monsoon system. These systems can effectively modulate the large-scale circulation through diabatic heating (Yuan and Houze, 2010; Hamada et al., 2014; Hoskins et al., 2019). In this study, we further investigate the changes in convective structures for both sets of simulations using the object-based analysis method (Tsai and Wu, 2017; Su et al., 2019; Wu and Chen, 2021). We apply the definition of the convective core clouds following Wu and Chen (2021) to identify the mature convective systems with updrafts. The size spectrum of the cloud objects is presented in Fig. 5a. The cloud objects during the early stages from the first day to half of the onset day are analyzed so that the early signals could be detected. The results show that the size spectrum of the experiments that lead to CA has a peak located at the size of about $10^{1.3}$ km^3, and the occurrence decreases with the increase of the size. The convective core clouds with sizes from 15.8 km^3 to 31.6 km^3 occur more frequently in VVM-Lin-agg. On the other hand, clouds larger than 31.6 km^3 are frequently found in P3-agg. The frequent occurrence of large-size convective systems in P3-all could drive a stronger mock-Walker circulation that enhances MCF.

The size spectrum differences due to the convective structure changes between experiments with VVM-Lin and P3 have been examined under strongly forced environments

(Huang and Wu, 2020). The P3 scheme can represent significant variabilities of ice particles between convective and stratiform cloud regions. In the convective updraft region, the cooling effects due to ice melting around the freezing level are reduced because of the rapid removal of fast-falling ice particles in the simulations with the P3 scheme. Then, the convective updraft will be stronger and produce more extreme precipitation when the P3 scheme is applied. The mechanism and results in Huang and Wu (2020) provide a lead to explain why the convective systems are more organized in P3-all.

We sample the grid boxes inside the convective core clouds with the same period as Fig. 5a to derive the contoured frequency by altitude diagrams (CFAD) of vertical velocity for VVM-Lin-agg (Fig. 5b) and P3-agg (Fig. 5c). A top-heavy structure is shown in both VVM-Lin-agg and P3-agg. Above 500 hPa, the contours of the frequency in VVM-Lin-agg (Fig. 5b) shifts towards the moderate vertical velocity region (5 m s^{-1} ~ 10 m s^{-1}) when the altitude increases. This indicates that the convective updraft decelerates as ice-phase processes are involved, and the weakening starting from the freezing level is consistent with the melting effects in Huang and Wu (2020). On the other hand, P3-agg has a wider distribution of the frequency in the upper level (Fig. 5c), and the distribution extends to the more extreme region (35 m s^{-1}). The results show that the convective updraft is stronger in P3-agg because of the reduced melting effects. The change in the convective structures due to the reduced melting effect in P3-all could increase the occurrence of large-size convective systems. Then, these systems enhance the mock-Walker circulation, and stronger MCF leads to the easier development of CA in P3-all compared to VVM-Lin-all.

5 Summary

In this study, we propose a framework to evaluate convective aggregation (CA) in radiative convective equilibrium simulations and demonstrate the framework with examples of two different microphysics schemes. The framework introduces a mixed-layer slab ocean with an initial SST gradient to design the competition between moisture-convection feedback (MCF) and convection-SST feedback (CSF) induced by the mock-Walker circulation and low-level circulation, respectively. Two sets of simulations are performed using the vector vorticity equation cloud-resolving model (VVM) with the conventional category-based (VVM-Lin) and the predicted particle properties (P3) microphysics schemes. A clear bifurcation of the aggregated/non-aggregated states can be identified in both sets of experiments. In the phase diagram constructed with the initial SST gradient and the mixed-layer depth, the boundary of the bifurcation can be identified in both sets of experiments. The bifurcation line of P3-all is located at the lower-left part of the phase diagram, which indicates stronger MCF in P3-all compared to that in VVM-Lin-all. These two sets of simulations exhibiting different bifurcation lines is a clear demonstration that our framework can effectively identify how the two feedbacks compete with each other during the development of CA among different models. The results are further quantified using the frozen moist static energy variance budget.

We provide examples with different microphysical parameterizations using the same model in this study. However, various factors can influence CA, and it is necessary to investigate what causes the differences among cloud-resolving models in RCE simulations. The framework designed based on the competing effects between MCF and CSF provides a physical-based evaluation of CA. Currently, an intercomparison between VVM and a regional model constructed with Scalable Computing for Advanced Library and Environment (SCALE, Nishizawa et al., 2015; Sato et al., 2015) is conducted for RCE experiments. The preliminary results show that these two CRMs have very different pathways toward CA. We will apply this framework to quantify the competing effects between MCF and CSF in this intercomparison to obtain process-oriented explanations of model differences.

Acknowledgments

We thank Prof. Wei-Ting Chen and Mr. Chun-Yian Su for providing valuable discussions on this study. Jin-De Huang and Chien-Ming Wu were supported by Taiwan's MoST through Grant 107-2111-M-002-010-MY4 and Academia Sinica through Grant AS-TP-109-M11 to National Taiwan University. The analyzing codes and post-processing data are available in the online open-access repository (https://doi.org/10.6084/m9.figshare.16628692.v1).

Reference

Arakawa, A., & Wu, C.-M. (2013). A unified representation of deep moist convection in numerical modeling of the atmosphere. Part I. Journal of the Atmospheric Sciences, 70(7), 1977–1992. https://doi.org/10.1175/JAS-D-12-0330.1

Bretherton, C. S., & Sobel, A. H. (2002). A simple model of a convectively coupled Walker circulation using the weak temperature gradient approximation. Journal of Climate, 15(20), 2907-2920. https://doi.org/10.1175/1520-0442(2002)015<2907:ASMOAC>2.0.CO;2

Bretherton, C. S., Blossey, P. N., & Khairoutdinov, M. (2005). An energy-balance analysis of deep convective self-aggregation above uniform SST. Journal of the Atmospheric Sciences, 62, 4273–4292. https://doi.org/10.1175/JAS3614.1

Bretherton, C.S., Blossey, P.N. & Peters, M.E. (2006). Interpretation of simple and cloud-resolving simulations of moist convection–radiation interaction with a mock-Walker circulation. Theoretical and Computational Fluid Dynamics, 20, 421–442. https://doi.org/10.1007/s00162-006-0029-7

Byrne, M. P., & Schneider, T. (2016). Energetic constraints on the width of the intertropical convergence zone. Journal of Climate, 29(13), 4709-4721. https://doi.org/10.1175/JCLI-D-15-0767.1

Chang, Y.-H., Chen, W.-T., Wu, C.-M., Moseley, C., & Wu, C.-C. (2021). Tracking the influence of cloud condensation nuclei on summer diurnal precipitating systems over complex topography in Taiwan. Atmospheric Chemistry and Physics. Discuss. https://doi.org/10.5194/acp-2021-113

Chen, F., & Dudhia, J. (2001). Coupling an advanced land surface–hydrology model with the Penn State–NCAR MM5 modeling system. Part I: model implementation and sensitivity. Monthly Weather Review, 129(4), 569-585. https://doi.org/10.1175/1520-0493(2001)129<0569:CAALSH>2.0.CO;2

Chen, P.-J., Chen, W.-T., Wu, C.-M., & Yo, T.-S. (2021). Convective cloud regimes from a classification of object-based CloudSat observations over Asian-Australian monsoon areas. Geophysical Research Letters, 48, e2021GL092733. https://doi.org/10.1029/2021GL092733

Chen, W.-T., Wu, C.-M., Tsai, W.-M., Chen, P.-J., & Chen, P.-Y. (2019). Role of coastal convection to moisture buildup during the South China Sea summer monsoon onset. Journal of the Meteorological Society of Japan, 97(6), 1155-1171. https://doi.org/10.2151/jmsj.2019-065

Chen, Y.-T., & Wu, C.-M. (2019). The role of interactive SST in the cloud-resolving simulations of aggregated convection. Journal of Advances in Modeling Earth Systems, 11, 3321–3340. https://doi.org/10.1029/2019MS001762

Chien, M.-H., & Wu, C.-M. (2016). Representation of topography by partial steps using the immersed boundary method in a vector vorticity equation model (VVM). Journal of Advances in Modeling Earth Systems, 8, 212–223. https://doi.org/10.1002/2015MS000514

Craig, G. C., & Mack, J. M. (2013). A coarsening model for self-organization of tropical convection. Journal of Geophysical Research, Atmospheres, 118, 8761–8769. https://doi.org/10.1002/jgrd.50674

Cronin, T. W., & Wing, A. A. (2017). Clouds, circulation, and climate sensitivity in a radiative-convective equilibrium channel model. Journal of Advances in Modeling Earth Systems, 9, 2883– 2905. https://doi.org/10.1002/2017MS001111

Coppin, D., & Bony, S. (2015). Physical mechanisms controlling the initiation of convective self-aggregation in a general circulation model. Journal of Advances in Modeling Earth Systems, 7, 2060–2078. https://doi.org/10.1002/2015MS000571

Emanuel, K., Wing, A. A., & Vincent, E. M. (2014). Radiative-convective instability. Journal of Advances in Modeling Earth Systems, 6, 75– 90, http://doi.org/10.1002/2013MS000270

Grabowski, W. W., Yano, J., & Moncrieff, M. W. (2000). Cloud resolving modeling of tropical circulations driven by large-scale SST gradients. Journal of the Atmospheric Sciences, 57(13), 2022-2040. https://doi.org/10.1175/1520-0469(2000)057<2022:CRMOTC>2.0.CO;2

Grabowski, W.W., & Moncrieff, M.W. (2001). Large-scale organization of tropical convection in two-dimensional explicit numerical simulations. Quarterly Journal of the Royal Meteorological Society, 127: 445-468. https://doi.org/10.1002/qj.49712757211

Grabowski, W.W., & Moncrieff, M.W. (2004). Moisture–convection feedback in the tropics. Quarterly Journal of the Royal Meteorological Society, 130: 3081-3104. https://doi.org/10.1256/qj.03.135

Grabowski, W. W. (2006). Impact of Explicit Atmosphere–Ocean Coupling on MJO-Like Coherent Structures in Idealized Aquaplanet Simulations. Journal of the Atmospheric Sciences, 63(9), 2289-2306. https://doi.org/10.1175/JAS3740.1

Hamada, A., Murayama, Y., & Takayabu, Y. N. (2014). Regional Characteristics of Extreme Rainfall Extracted from TRMM PR Measurements. Journal of Climate, 27(21), 8151-8169. https://doi.org/10.1175/JCLI-D-14-00107.1

Held, I. M., Hemler, R. S., & Ramaswamy, V. (1993). Radiative-Convective Equilibrium with Explicit Two-Dimensional Moist Convection. Journal of Atmospheric Sciences, 50(23), 3909-3927. https://doi.org/10.1175/1520-0469(1993)050<3909:RCEWET>2.0.CO;2

Hohenegger, C., & Stevens, B. (2016). Coupled radiative convective equilibrium simulations with explicit and parameterized convection. Journal of Advances in Modeling Earth Systems, 8, 1468– 1482. https://doi.org/10.1002/2016MS000666

Holloway, C. E., & Neelin, J. D. (2010). Temporal relations of column water vapor and tropical precipitation. Journal of the Atmospheric Sciences, 67(4), 1091-1105. https://doi.org/10.1175/2009JAS3284.1

Holloway, C. E., & Woolnough, S. J. (2016). The sensitivity of convective aggregation to diabatic processes in idealized radiative-convective equilibrium simulations. Journal of Advances in Modeling Earth Systems, 8, 166– 195. https://doi.org/10.1002/2015MS000511

Holloway, C. E., Wing, A. A., Bony, S., Muller, C., Masunaga, H., L'Ecuyer, T. S., et al. (2017). Observing convective aggregation. Surveys in Geophysics, 38, 1199–1236. https://doi.org/10.1007/s10712-017-9419-1

Hoskins, B. J., Yang, G. Y., & Fonseca, R. M. (2019). The detailed dynamics of the June-August Hadley Cell. Quarterly Journal of the Royal Meteorological Society, 146(727), 557–575. https://doi.org/10.1002/qj.3702

Huang, J.-D., & Wu, C.-M. (2020). Effects of microphysical processes on the precipitation Spectrum in a strongly forced environment. Earth and Space Science, 7, e2020EA001190. https://doi.org/10.1029/2020EA001190

Iacono, M. J., Delamere, J. S., Mlawer, E. J., Shephard, M. W., Clough, S. A., & Collins, W. D. (2008), Radiative forcing by long-lived greenhouse gases: Calculations with the AER radiative transfer models. Journal of Geophysical Research, 113, D13103. https://doi.org/10.1029/2008JD009944

Jung, J.-H., & Arakawa, A. (2008). A three-dimensional anelastic model based on the vorticity equation. Monthly Weather Review., 136(1), 276–294. https://doi.org/10.1175/2007MWR2095.1

Khairoutdinov, M. F., & Emanuel, K. A. (2010). Aggregated convection and the regulation of tropical climate, paper presented at 29th Conference on Hurricanes and Tropical Meteorology. Am. Meteorol. Soc., Tucson, Ariz.

Krueger, S. K., Fu, Q., Liou, K., & Chin, H.-N. S. (1995). Improvements of an ice-phase microphysics parameterization for use in numerical simulations of tropical convection. Journal of Applied Meteorology, 34(1), 281–287. https://doi.org/10.1175/1520-0450-34.1.281

Kuo, K.-T., & Wu, C.-M. (2019). The precipitation hotspots of afternoon thunderstorms over the Taipei Basin: Idealized numerical simulations. Journal of the Meteorological Society of Japan, 97(2), 501–517. https://doi.org/10.2151/jmsj.2019-031

Liu, C., & Moncrieff, M. W. (2008). Explicitly simulated tropical convection over idealized warm pools. Journal of Geophysical Research, Atmospheres, 113, D21121. https://doi.org/10.1029/2008JD010206

Mauritsen, T., & Stevens, B. (2015). Missing iris effect as a possible cause of muted hydrological change and high climate sensitivity in models. Nature Geoscience, 8, 346–351. https://doi.org/10.1038/ngeo2414

Muller, C. J., & Held, I. M. (2012). Detailed investigation of the self-aggregation of convection in cloud-resolving simulations. Journal of the Atmospheric Sciences, 69, 2551–2565. https://doi.org/10.1175/JAS-D-11-0257.1

Muller, C. J., & Bony, S. (2015). What favors convective aggregation and why? Geophysical Research Letters, 42, 5626–5634. https://doi.org/10.1002/2015GL064260

Morrison, H., & Milbrandt, J. A. (2015). Parameterization of ice microphysics based on the prediction of bulk particle properties. Part I: Scheme description and idealized tests. Journal of the Atmospheric Sciences, 72, 287–311. https://doi.org/10.1175/JAS-D-14-0065.1

Nishizawa, S., Yashiro, H., Sato, Y., Miyamoto, Y., & Tomita, H. (2015). Influence of grid aspect ratio on planetary boundary layer turbulence in large-eddy simulations. Geoscientific Model Development, 8(10), 3393–3419. https://doi.org/10.5194/gmd-8-3393-2015

Reed, A. K., Medeiros, B., Bacmeister, J. T., & Lauritzen, P. H. (2015). Global radiative-convective equilibrium in the Community Atmosphere Model Version 5. Journal of the Atmospheric Sciences, 72, 2183–2197. https://doi.org/10.1175/JAS-D-14-0268.1

Sato, Y., Nishizawa, S., Yashiro, H., Miyamoto, Y., Kajikawa, Y., & Tomita, H. (2015). Impacts of cloud microphysics on trade wind cumulus: Which cloud microphysics processes contribute to the diversity in a large eddy simulation? Progress in Earth and Planetary Science, 2(1), 23. https://doi.org/10.1186/s40645-015-0053-6

Su, C.-Y., Wu, C.-M., & Chen, W.-T. (2019). Object-based precipitation system bias in grey zone simulation: the 2016 South China Sea summer monsoon onset. Climate Dynamics, 53, 617–630. https://doi.org/10.1007/s00382-018-04607-x

Tompkins, A. M., & Craig, G. C. (1998). Radiative-convective equilibrium in a three-dimensional cloud-ensemble model. Quarterly Journal of the Royal Meteorological Society, 124, 2073–2097. https://doi.org/10.1002/qj.49712455013

Tompkins, A. (2001). Organization of tropical convection in low wind shears: The role of water vapor. Journal of the Atmospheric Sciences, 58, 529–545. https://doi.org/10.1175/1520-0469(2001)058<0529:OOTCIL>2.0.CO;2

Tompkins, A. M., & Semie, A. G. (2017). Organization of tropical convection in low vertical wind shears: Role of updraft entrainment. Journal of Advances in Modeling Earth Systems, 9, 1046–1068. https://doi.org/10.1002/2016MS000802

Tompkins, A. M., & Semie, A. G. (2021). Impact of a mixed ocean layer and the diurnal cycle on convective aggregation. Journal of Advances in Modeling Earth Systems, 13, e2020MS002186. https://doi.org/10.1029/2020MS002186

Tsai, J.-Y., & Wu, C.-M. (2016). Critical transitions of stratocumulus dynamical systems due to perturbation in free atmosphere moisture. Dynamics of Atmospheres and Oceans, 76, 1–13. https://doi.org/10.1016/j.dynatmoce.2016.08.002

Tsai, W.-M., & Wu, C.-M. (2017). The environment of aggregated deep convection. Journal of Advances in Modeling Earth Systems, 9, 2061–2078, https://doi.org/10.1002/2017MS000967.

Wing, A. A., & Emanuel, K. (2014). Physical mechanisms controlling self-aggregation of convection in idealized numerical modeling simulations. Journal of Advances in Modeling Earth Systems, 6, 59–74. https://doi.org/10.1002/2013MS000269

Wing, A. A., & Cronin, T. W. (2016). Self-aggregation of convection in long channel geometry. Quarterly Journal of the Royal Meteorological Society, 142, 1–15. https://doi.org/10.1002/qj.2628

Wing, A. A., Emanuel, K., Holloway, C. E., & Muller, C. (2017). Convective self-aggregation in numerical simulations: A review. Surveys in Geophysics, 38, 1173–1197. https://doi.org/10.1007/s10712-017-9408-4

Wing, A. A., Reed, K. A., Satoh, M., Stevens, B., Bony, S., & Ohno, T. (2018). Radiative-Convective Equilibrium Model Intercomparison Project. Geoscientific Model Development, 11, 793–813. https://doi.org/10.5194/gmd-11-793-2018

Wing, A.A. (2019). Self-aggregation of deep convection and its implications for climate. Current Climate Change Reports, 5, 1–11. https://doi.org/10.1007/s40641-019-00120-3

Wing, A. A., Stauffer, C. L., Becker, T., Reed, K. A., Ahn, M.-S., & Arnold, N. P., et al. (2020). Clouds and convective self-aggregation in a multimodel ensemble of radiative-convective equilibrium simulations. Journal of Advances in Modeling Earth Systems, 12(9), 1942-2466. https://doi.org/10.1029/2020MS002138

Wofsy, J., & Kuang, Z. (2012). Cloud-Resolving Model Simulations and a Simple Model of an Idealized Walker Cell. Journal of Climate, 25(23), 8090-8107. https://doi.org/10.1175/JCLI-D-11-00692.1

Wu, C.-M., & Arakawa, A. (2011). Inclusion of surface topography into the vector vorticity equation model (VVM). Journal of Advances in Modeling Earth Systems, 3, M04002. https://doi.org/10.1029/2011MS000061

Wu, C.-M., & Arakawa, A. (2014). A unified representation of deep moist convection in numerical modeling of the atmosphere. Part II. Journal of the Atmospheric Sciences, 71(6), 2089–2103. https://doi.org/10.1175/JAS-D-13-0382.1

Wu, C.-M., Lo, M.-H., Chen, W.-T., and Lu, C.-T. (2015), The impacts of heterogeneous land surface fluxes on the diurnal cycle precipitation: A framework for improving the GCM representation of land-atmosphere interactions, Journal of Geophysical Research, Atmospheres, 120, 3714–3727. https://doi.org/10.1002/2014JD023030

Wu, C.-M., Lin, H.-C., Cheng, F.-Y., & Chien, M.-H. (2019). Implementation of the land surface processes into a vector vorticity equation model (VVM) to study its impact on afternoon thunderstorms over complex topography in Taiwan. Asia-Pacific Journal of Atmospheric Sciences. https://doi.org/10.1007/s13143-019-00116-x

Wu, C.-M., & Chen, P.-Y. (2021). Idealized cloud-resolving simulations of land-atmosphere coupling over tropical islands. Terrestrial, Atmospheric and Oceanic sciences journal, in press. https://doi.org/ 10.3319/TAO.2020.12.16.01

Yanase, T., Nishizawa, S., Miura, H., Takemi, T., & Tomita, H. (2020). New critical length for the onset of self-aggregation of moist convection. Geophysical Research Letters, 47, e2020GL088763. https://doi.org/10.1029/2020GL088763

Yuan, J., & Houze, R. A., Jr. (2010). Global variability of mesoscale convective system anvil structure from A-train satellite data. Journal of Climate, 23(21), 5864–5888. https://doi.org/10.1175/2010JCLI3671.1

Figure and Table

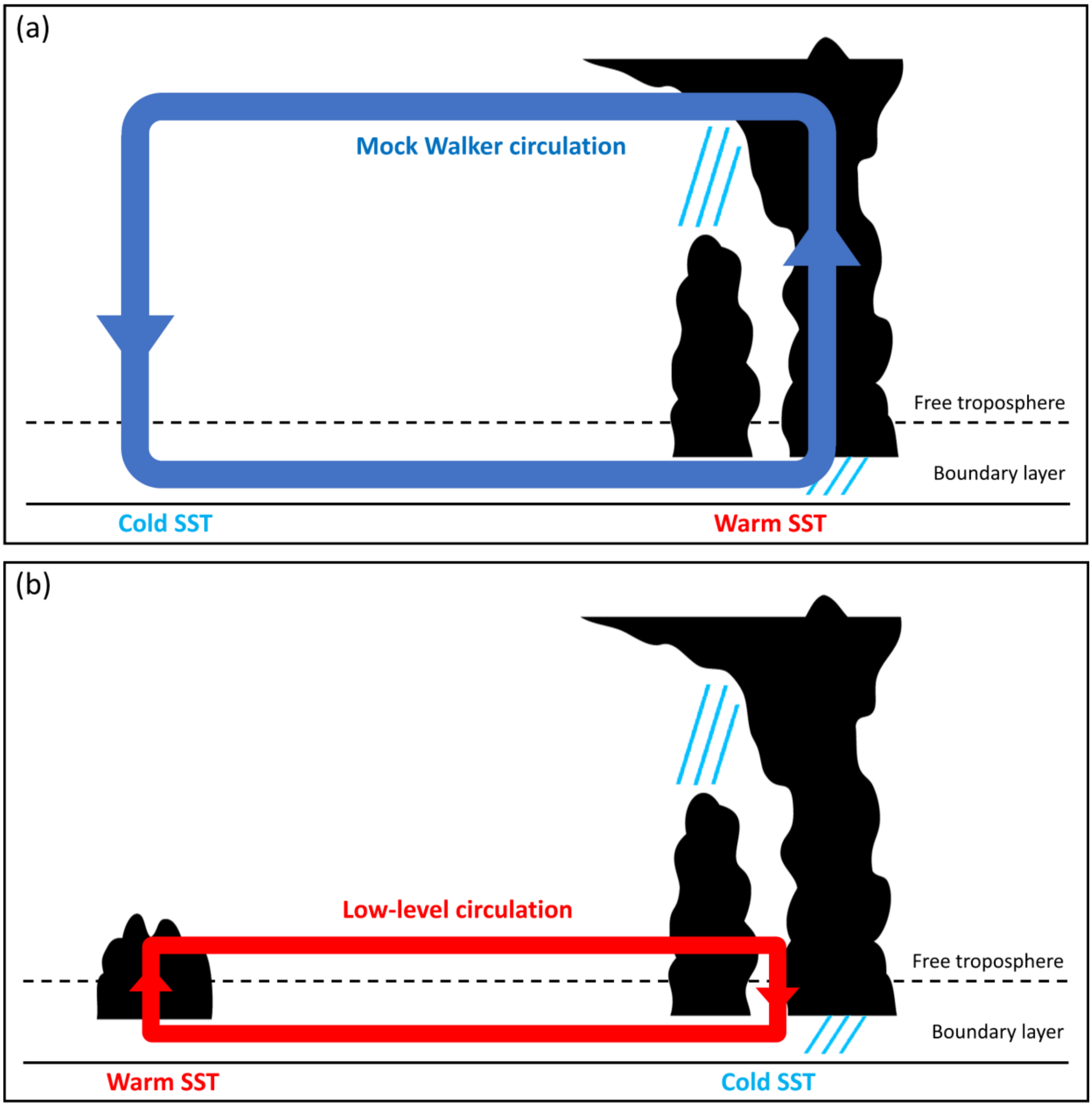

Figure 1. The schematics of the moisture-convection and convection-SST feedbacks. See text for more details.

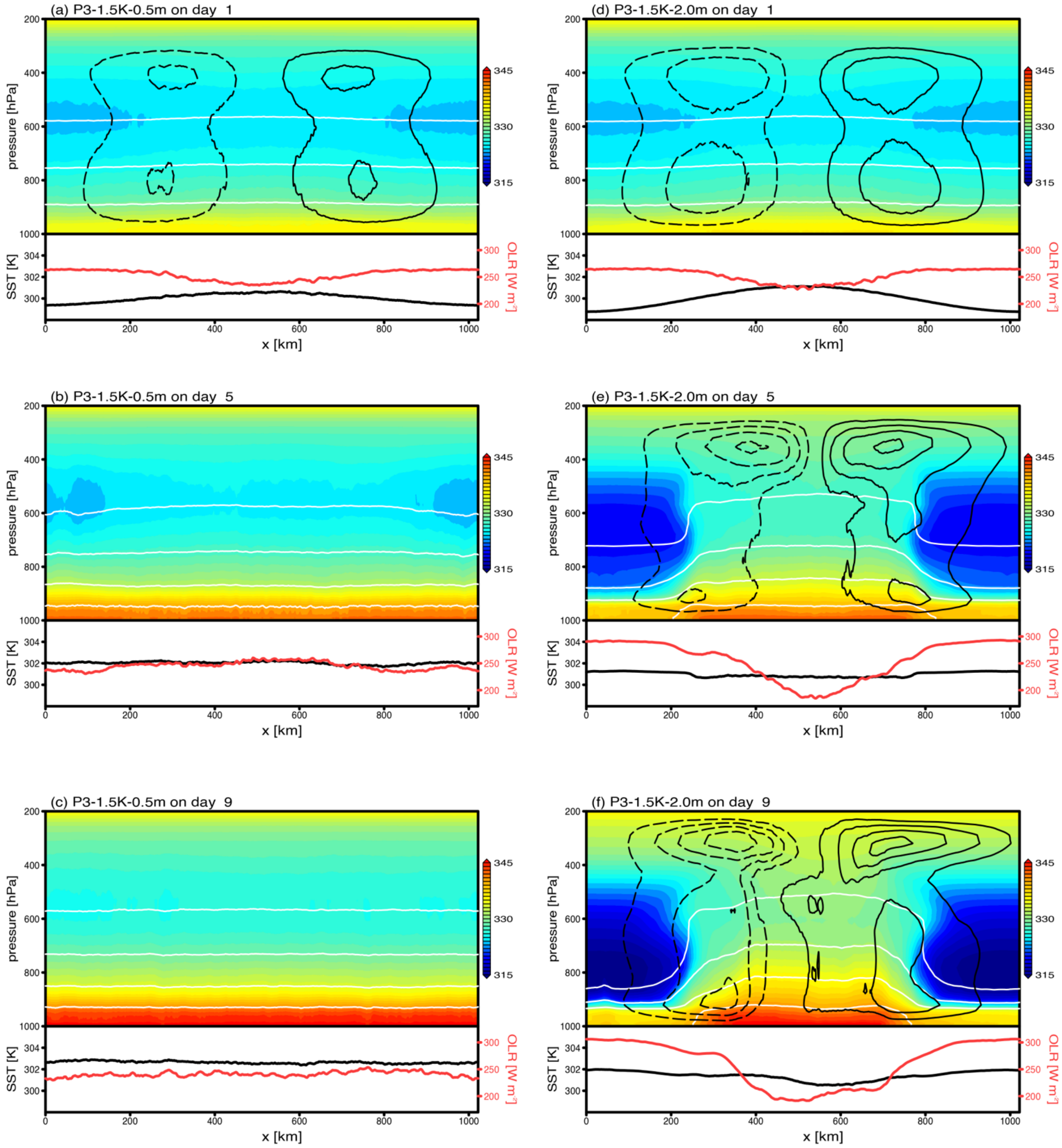

Figure 2. Daily and meridionally averaged FMSE (color shading), mass streamfunction (black contours), and water vapor mixing ratio (white contours) for P3-1.5K-0.5m and P3-1.5K-2.0m on days 1, 5, and 9. Daily-averaged SST and OLR are shown in the bottom part of each panel.

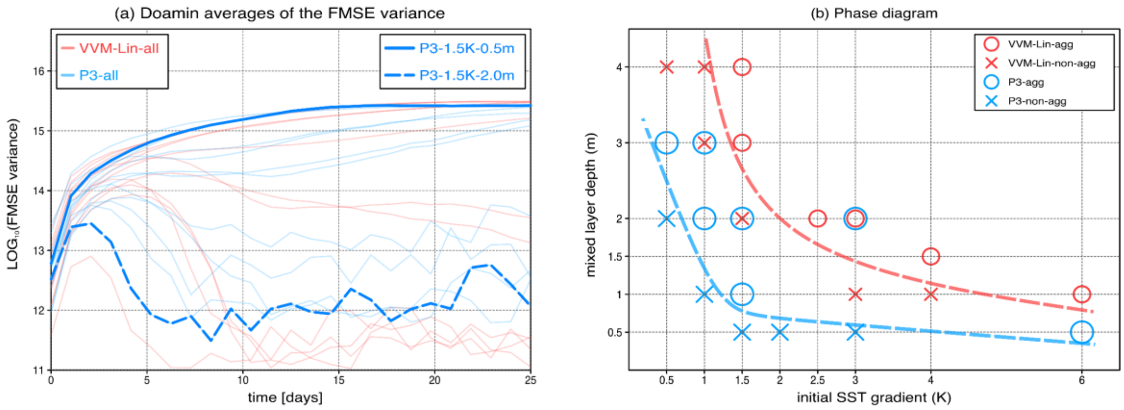

Figure 3. (a) The time evolutions of the domain-averaged FMSE variance are presented by the attenuated red (VVM-Lin-all) and cyan (P3-all) lines. P3-1.5K-0.5m and P3-1.5K-2.0m are emphasized by the thick solid and dash lines, respectively. (b) The phase diagram of experiments results with respect to their initial SST gradient and mixed-layer depth. The increase of the x-axis and the y-axis represents the strengthening of MCF and the weakening of CSF, which promotes CA. Circles and crosses represent the aggregated and non-aggregated states, respectively. The dashed lines indicate the transition of the states with/without the development of CA in VVM-Lin-all (red) and P3-all (cyan).

577

578

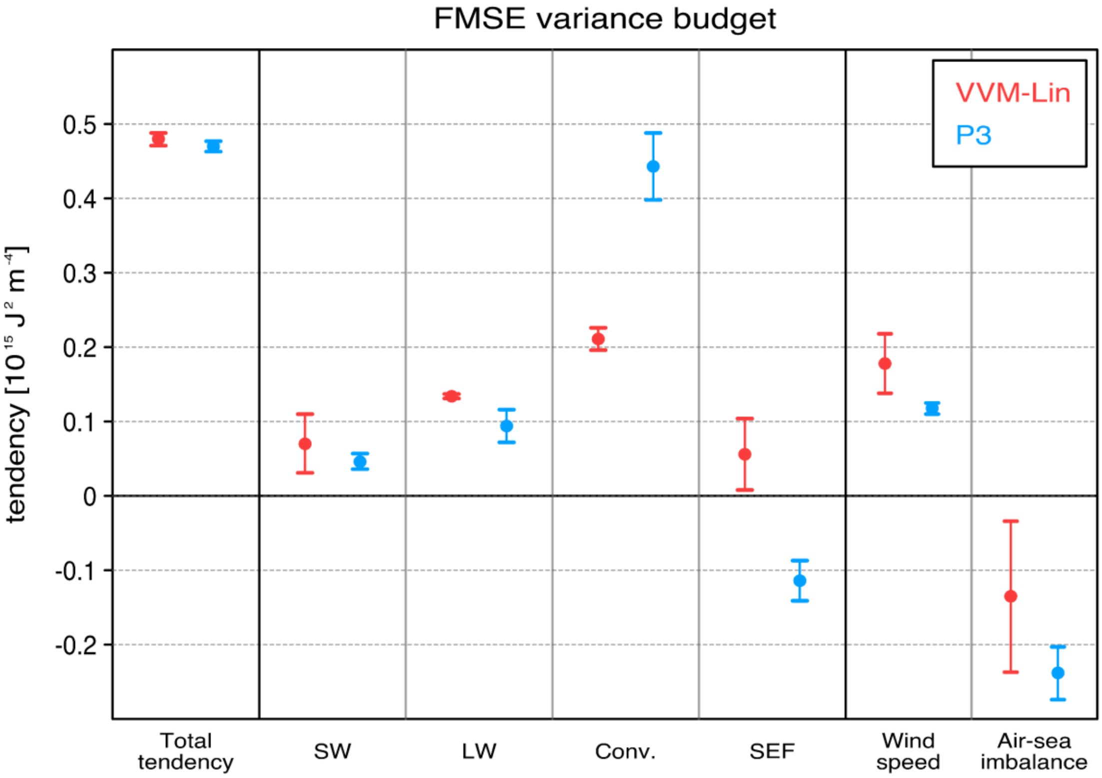

Figure 4. The FMSE variance budget analysis of the spatial FMSE variance of VVM-Lin-agg (red) and P3-agg (cyan). The first column is the total tendency which is the left-hand-side term in Eq. (3), and the following four columns are the right-hand-side terms in Eq. (3). The final two columns are the wind speed anomaly and air-sea imbalance terms that decomposed from SEF. Dots represent the averages of each term, and the bars indicate the standard deviations.

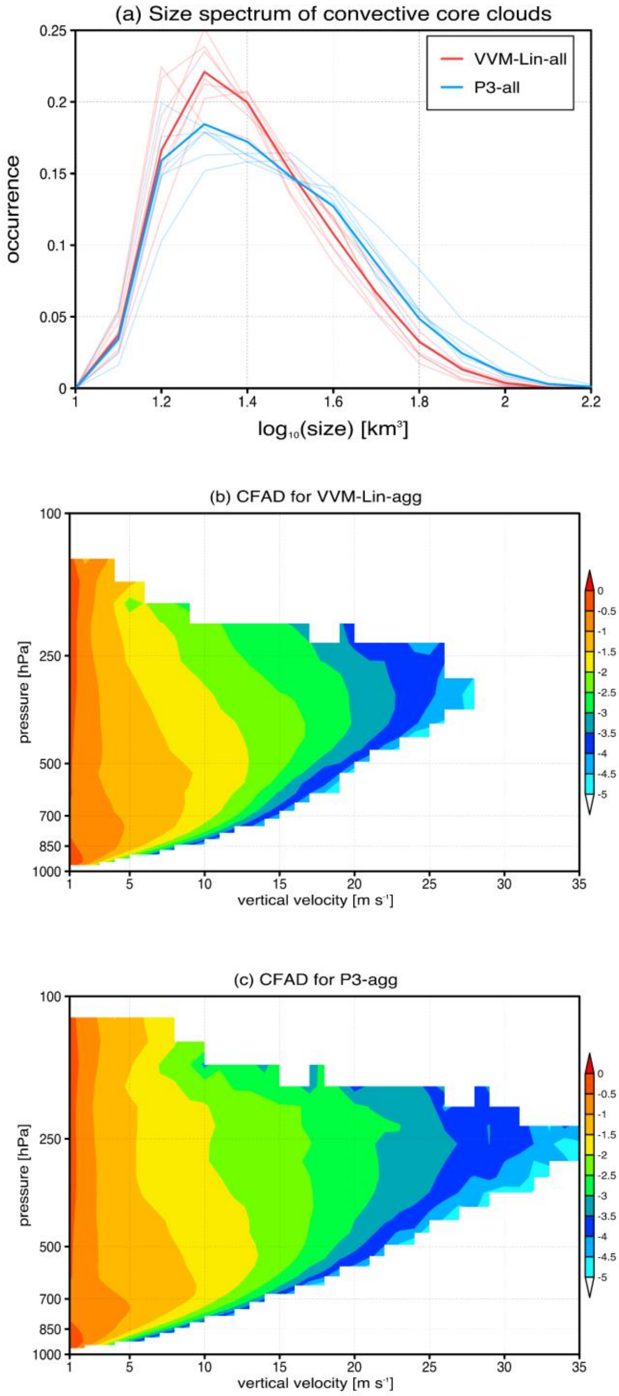

Figure 5. (a) The size distribution of the convective core clouds sampled from the first day to half of the onset day, and the summation of the occurrence for each line is unity. The red and cyan thick lines, respectively, represent the averages of VVM-Lin-agg and P3-agg, and the attenuated lines are the size distribution for each simulation. The contoured frequency by altitude diagram (CFAD) of vertical velocity in logarithmic scale for VVM-Lin-agg (b) and P3-agg (c).

Experiments	Aggregation	Onset days	Experiments	Aggregation	Onset days
VVM-Lin-3.0K-2.0m	Yes	7	P3-1.5K-2.0m	Yes	7
VVM-Lin-1.5K-2.0m	No	-	P3-1.0K-1.0m	No	-
VVM-Lin-3.0K-1.0m	No	-	P3-2.0K-0.5m	No	-
VVM-Lin-1.5K-4.0m	Yes	9	P3-3.0K-2.0m	Yes	9
VVM-Lin-6.0K-1.0m	Yes	8	P3-3.0K-0.5m	Yes	8
VVM-Lin-1.5K-3.0m	Yes	19	P3-6.0K-0.5m	Yes	19
VVM-Lin-1.0K-3.0m	No	-	P3-1.0K-2.0m	No	-
VVM-Lin-4.0K-1.5m	Yes	7	P3-0.5K-3.0m	Yes	7
VVM-Lin-4.0K-1.0m	No	-	P3-0.5K-2.0m	No	-
VVM-Lin-0.5K-4.0m	No	-	P3-1.5K-0.5m	No	-
VVM-Lin-1.0K-4.0m	No	-	P3-1.5K-1.0m	No	-
VVM-Lin-2.5K-2.0m	Yes	9	P3-1.0K-3.0m	Yes	9

Table 1. The list of the simulations, their equilibrium states with/without CA, and the onset days of CA.